

The LaGrange Tornado during VORTEX2. Part II: Photogrammetric Analysis of the Tornado Combined with Dual-Doppler Radar Data

NOLAN T. ATKINS, ANTHONY MCGEE, AND RACHEL DUCHARME

Department of Atmospheric Sciences, Lyndon State College, Lyndonville, Vermont

ROGER M. WAKIMOTO

National Center for Atmospheric Research, Boulder, Colorado*

JOSHUA WURMAN

Center for Severe Weather Research, Boulder, Colorado

(Manuscript received 19 October 2011, in final form 21 February 2012)

ABSTRACT

This study presents the synthesis of dual-Doppler and cloud photography data of the 5 June 2009 Goshen County, Wyoming, tornado observed during the Second Verification of the Origins of Rotation in Tornadoes Experiment (VORTEX2). Analyses focused on the hook region of the parent supercell. It will be shown that radar-determined tornadogenesis and initial surface wind damage occurred 14 min before the funnel cloud was observed continuously on the ground. In addition to the cyclonic wall cloud, an anticyclonic lowering was also observed on the southern flank of the hook echo near the time of tornadogenesis.

The relationship between the intensities of the tornado and its parent circulation, the low-level mesocyclone, will also be discussed. Funnel diameter was not well correlated with the maximum vertical vorticity or circulation associated with the mesocyclone. Furthermore, changes in the minimum reflectivity observed in the tornado-scale weak echo hole (WEH) were weakly correlated with the maximum vertical vorticity of the mesocyclone. The tornado funnel was observed within and was relatively small compared to the WEH diameter.

The distribution and evolution of angular momentum were also examined. The radial increase of angular momentum terminated at or beyond the wall cloud edge. Prior to the time that the funnel made continuous contact with the ground, low-level angular momentum increased despite the fact that azimuthally averaged low-level flow within the mesocyclone was divergent, advecting low angular momentum air away from the circulation center. Both the tornado and mesocyclone generally intensified during this time. Thereafter, while the tornado continued to intensify, angular momentum within the low-level mesocyclone weakened.

1. Introduction

Beginning with the seminal study by Stout and Huff (1953), the close association between the supercell hook echo and tornadoes has been well established in the literature. The tornado often forms within a larger-scale circulation often referred to as either the low-level

mesocyclone or tornado cyclone. Low-level mesocyclones have been well observed with Doppler radars (e.g., Bluestein and Unruh 1989; Bluestein et al. 1997; Wurman et al. 1997; Dowell and Bluestein 1997, 2002a,b; Wakimoto and Liu 1998; Trapp 1999; Wakimoto and Cai 2000; Wurman and Gill 2000; Bluestein and Pazmany 2000; Bluestein and Gaddy 2001; Bluestein et al. 2003, 2004; Alexander and Wurman 2005; Wurman and Alexander 2005; Beck et al. 2006; Tanamachi et al. 2007; Wurman et al. 2007b,c; Marquis et al. 2008; French et al. 2008; Wurman et al. 2008; Frame et al. 2009; Wurman et al. 2010) and studied in numerical simulations (e.g., Klemp and Rotunno 1983; Rotunno and Klemp 1985; Davies-Jones and Brooks 1993). Mesocyclone core diameters vary from about 3–9 km (Davies-Jones et al.

* The National Center for Atmospheric Research is sponsored by the National Science Foundation.

Corresponding author address: Nolan T. Atkins, Department of Atmospheric Sciences, Lyndon State College, Lyndonville, VT 05851.

E-mail: nolan.atkins@lyndonstate.edu

2001). Their genesis has been attributed to tilting and subsequent stretching of solenoidally generated horizontal vorticity (e.g., Rotunno and Klemp 1985; Davies-Jones and Brooks 1993; Markowski et al. 2008). Tornado cyclones have a spatial scale smaller than the low-level mesocyclone and larger than the tornado (Agee et al. 1976). They have been defined as the region surrounding the tornado where angular momentum increases radially outward and a certain degree of axisymmetry is maintained (Rasmussen and Straka 2007). It is possible, however, that the tornado cyclone is simply an unusually compact, intense low-level mesocyclone. No robust dynamical distinction between low-level mesocyclones and tornado cyclones has been documented in the literature.

Visually, the low-level mesocyclone is thought to be associated with the wall cloud, a lowering of the cloud base near the storm updraft (Rotunno and Klemp 1985; Davies-Jones 1986; Bluestein 1993). It has long been recognized by storm intercept teams that the wall cloud is a possible precursor to tornadogenesis (Wakimoto and Liu 1998). Little is known, however, about the visual evolution and structure of the wall cloud relative to either the tornado or the low-level mesocyclone.

Observations of the tornado have become more numerous in recent years as ground-based mobile Doppler radars have been able to resolve the tornadic flow when scanning at close range (e.g., Wurman et al. 1996; Wurman and Gill 2000; Bluestein et al. 2003; Alexander and Wurman 2005; Wurman et al. 2007b,c). Many interesting features related to the tornado and possibly tornadogenesis within the hook region have been observed with mobile Doppler radars such as weak echo holes (e.g., Fujita 1981; Wakimoto and Martner 1992; Wakimoto et al. 1996; Wurman and Gill 2000; Bluestein and Pazmany 2000; Bluestein et al. 2003, 2004, 2007b; Wurman et al. 2007b, 2010), reflectivity knobs (Burgess et al. 2002), debris rings (e.g., Wurman et al. 1996; Wurman and Gill 2000; Wurman et al. 2007c; Tanamachi et al. 2007; Wurman et al. 2010), debris (Ryzhkov et al. 2005; Bluestein et al. 2007b), multiple vortices (Wurman and Gill 2000), and secondary rear-flank gust fronts (Wurman et al. 2007b; Marquis et al. 2008; Wurman et al. 2010).

Despite the increasing number of observations in the supercell hook region, the visual relationship between the tornado and low-level mesocyclone remains poorly understood. This can, in part, be attributed to the lack of high-resolution concurrent observations of the tornado and low-level mesocyclone during the lifetime of the tornado.

To address this problem, high-resolution photographs of a tornado formed on 5 June 2009 over southeastern Wyoming were combined photogrammetrically with concurrent high-resolution Doppler radar data collected as part of the Second Verification of the Origins of

Rotation in Tornadoes Experiment (VORTEX2; Wurman et al. 2010). These observations are unique in that data collection began well before tornadogenesis and continued through nearly the entire life cycle of the tornado. Previous studies (e.g., Bluestein et al. 1997, 2004, 2007a,b; Wakimoto et al. 2003; Dowell et al. 2005; Rasmussen and Straka 2007) have combined tornado photographs with Doppler radar data; however, for only one or a few select times. The only comprehensive photogrammetric and Doppler radar analysis was presented by Wakimoto and Martner (1992); however, it was for a nonsupercell tornado.

In Part I of this study (Wakimoto et al. 2011, hereafter Part I), single Doppler radar data were combined with photographs to examine the structure of the weak echo hole (WEH) and rotational couplet to the visual characteristics of the tornado. In Part II, photographs of the wall cloud and tornado were combined with dual-Doppler data. The primary objective of Part II is to examine the relationship between the visual characteristics of the wall cloud and tornado with the low-level mesocyclone that was resolved in the dual-Doppler analysis. An overview of VORTEX2 along with the data and analysis techniques presented herein are discussed in section 2. The environmental conditions on 5 June 2009 and storm morphology are discussed in section 3. Section 4 presents results of the dual-Doppler radar and visual data synthesis, while conclusions are given in section 5.

2. VORTEX2, DOW radar data, and cloud photogrammetry

a. VORTEX2

VORTEX2 was a large multiagency field program that operated 10 May–13 June 2009 and 1 May–15 June 2010 and focused on collecting comprehensive datasets on tornadoes, the tornadic parent storm, and the environment within which it formed. To increase the number of storms for which data were collected, the experiment was mobile with no home base. The experiment employed 11 ground-based mobile radars, 14 mobile mesonet instrumented vehicles, 5 mobile balloon sounding systems, 38 deployable in situ weather stations, an unmanned aerial system, video and photogrammetry teams, damage survey teams, and portable laser disdrometers (Wurman et al. 2010). The VORTEX2 armada traveled nearly the entire High Plains from central Texas to southern North Dakota, covering approximately 16 000 and 25 000 km in 2009 and 2010, respectively. More information on VORTEX2 can be found in Wurman et al. (2010).

TABLE 1. Summary of relevant characteristics for the Doppler-on-Wheels 6 and 7 radars.

Transmitted frequency	9.37 GHz
Scan rate	$50^{\circ} \text{ s}^{-1}$
Pulse repetition frequency	4000 Hz
Pulse duration	400 ns
Gate spacing	60 m
Peak transmitted power	250 kW
Half-power beamwidth	0.93°

b. DOW radar data

The radar data used in this study were collected by the Doppler-on-Wheels (DOW) 6 and 7 platforms. Relevant parameters for DOW 6 and 7 are given in Table 1. The synchronous scanning between DOW 6 and 7 resulted in 2-min volume scan sets. In the first 45 s, surveillance scans at the 0.5° , 1.0° , 2.0° , 3.0° , 4.0° , 5.0° , and 6.0° elevation angles were collected. The next set of scans were collected at 0.5° , 1.0° , 2.0° , 8.0° , 10.0° , 12.0° , 14.0° , and 16.0° thus providing low-level updates every minute. The first 0.5° scan was not collected by DOW 7. All scans were used in the dual-Doppler synthesis except the second 0.5° , 1.0° , and 2.0° and 1.0° and 2.0° scans collected by DOW 6 and DOW 7, respectively.

DOW 6 and 7 reflectivity and radial velocity data were navigated using local ground clutter targets. All data were edited to remove ground clutter and the velocity data were unfolded. The resulting data were interpolated to a common Cartesian grid. The horizontal and vertical grid spacing was set to 100 m. The objective analysis was accomplished with a two-pass Barnes filter. The maximum range from both radars to the developing tornado was 20 km. This range was used to set the objective analysis smoothing. During the analysis times presented herein, the range to the tornado from DOW 6 and 7 varied from 20 to 15 and 20 to 5 km, respectively. Data were oversampled in the azimuthal direction (0.7°) resulting in a maximum horizontal data spacing (δ) of 0.244 km. The resultant horizontal smoothing parameter $\kappa [(=1.33\delta)^2]$ was 0.106 km^2 (Pauley and Wu 1990). The elevation angle increment was 1.0° resulting in a vertical smoothing parameter of 0.216 km^2 . The horizontal and vertical grid spacing ($\Delta = \delta/2.5$) were thus chosen to be 100 m (Koch et al. 1983). A second-pass convergence parameter of 0.3 was used based on the experiments of Majcen et al. (2008). No extrapolation was permitted during the objective analysis. During the dual-Doppler synthesis, data were often extrapolated downward from the lowest grid level with data to the lowest grid level ($z = 0$) by extrapolating the directional cosine coefficients in the dual-Doppler equation. Scan sequences between DOW 6 and DOW 7 were synchronized so that scans

through the storm were nearly contemporaneous. Low-level mesocyclone motion was used during the objective analysis to adjust data positions to the beginning time of the scan sequence and to compute dual-Doppler storm-relative winds. The resultant dual-Doppler data did not have the requisite resolution to well resolve the tornado. Using the above parameters, 50% and 80% of wave energy at scales greater than 0.63 and 0.95 km, respectively were resolved. Therefore, the dual-Doppler analysis well resolved the mesocyclone and many other features observed in the hook region of the supercell. Vertical velocities were derived from upward integration of the continuity equation setting $w = 0$ at the lower boundary. While it is common in dual-Doppler studies to generate the vertical velocity field by integrating the continuity equation, the vertical velocity field in this study should be interpreted with some caution. Because of the sampling limitations, it is likely that the low-level convergence field is not well resolved in the dual-Doppler data. Thin layers of low-level convergence are often observed in the vicinity of tornadoes. If this layer is not resolved in the dual-Doppler synthesis, erroneous negative vertical velocities may be generated near the circulation center.

c. Photogrammetry

Photogrammetry is the process of placing an accurate azimuth/elevation grid on a photo thus allowing the analyst to extract quantitative information such as the positions of clouds (e.g., Rasmussen et al. 2003; Zehnder et al. 2007). The photogrammetry process requires knowing the precise position of the photographer and the location of at least one distinguishable landmark on the horizon. Using spherical trigonometry, the effective focal length is then calculated for a panorama of pictures taken at the photo site (camera tilt angle = 0°). The azimuths of other distinguishable horizon landmarks in the panorama can then be found. With known azimuths of at least two landmarks in the photo of interest, the effective focal length and tilt angle of the camera lens can be computed and are used to produce the azimuth/elevation grid for the photo. Tests with known landmarks showed that the grids were accurate to within 0.1° – 0.2° . Image distortion was insignificant due to the quality of the camera lens and the fact that the analysis area and features of interest were located in the center part of the image where distortion is minimal.

All vertical cross sections of radar data superimposed on photos presented herein were taken in the plane of the photograph and at a range that passed through the vertical vorticity maximum in the dual-Doppler analysis at the respective level. For some analysis times, the horizontal location of the vertical vorticity maximum shifted slightly to the northeast with height resulting in

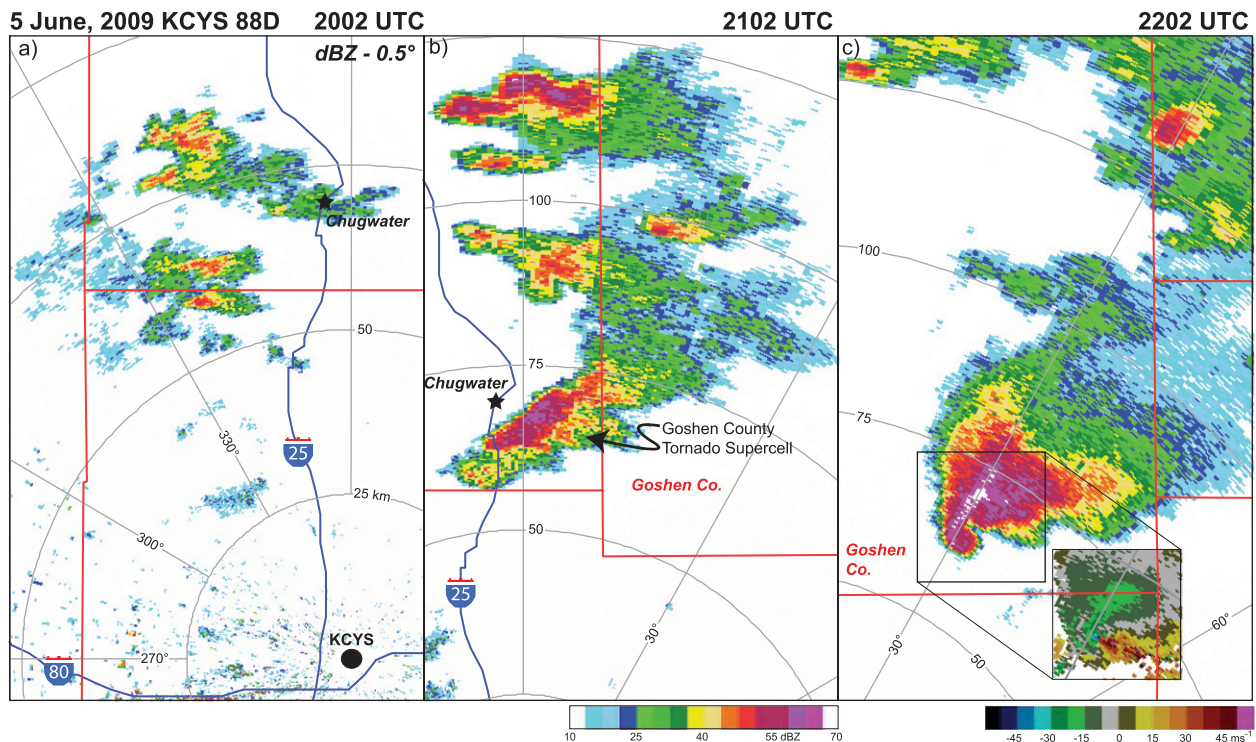


FIG. 1. Radar reflectivity (dBZ) data from the Cheyenne, WY, WSR-88D radar at (a) 2002, (b) 2102, and (c) 2202 UTC 5 Jun 2009. Ground-relative radial velocities are shown in the inset diagram in (c). All data are from the 0.5° elevation scan.

radar vertical cross sections that tilted to the northeast. More details on the photogrammetry process can be found in the appendix in Part I.

3. Environmental conditions and storm morphology

The VORTEX2 armada started the day on 5 June 2009 in Sterling, Colorado. After some discussion at the morning weather briefing, the targeted area was the region of the Nebraska Panhandle and southeastern Wyoming where favorable low-level and midlevel shear for tornadic supercells (Thompson et al. 2003) was forecast along with relatively high boundary layer moisture and lower convective temperatures. The convective available potential energy (CAPE) was anticipated to be greater than 1500 J kg^{-1} in this region. Convective initiation was anticipated in the upslope flow over the higher terrain northwest of Cheyenne, Wyoming.

At 2002 UTC (Fig. 1a), convection was initiating west of Chugwater, Wyoming, and moved to the east. Over the next hour, some of the cells had developed midlevel rotation. The VORTEX2 armada decided to target the southernmost storm located southeast of Chugwater (Fig. 1b). Many of the VORTEX2 teams began data collection on the storm as it moved into Goshen County at about

2130 UTC. By 2202 UTC, the targeted storm had developed a well-defined hook echo and intense rotational couplet (Fig. 1c). Note that 2202 UTC is 10 min after the time of DOW radar-determined tornadogenesis (2152 UTC). Based on numerous tornado intercepts by the DOWs, tornadogenesis was objectively determined to be when a 40 m s^{-1} radial velocity difference was first observed across the circulation with a diameter of 2 km or less (Alexander and Wurman 2008).

The rotational couplet location relative to DOW 7 and the camera team (CAMA) is shown in Fig. 2. At the time of tornadogenesis (2152 UTC), the couplet was located approximately 20 km to the west-northwest (WNW) of DOW 7. At this time, the tornado was producing minor damage, snapping tree limbs and uprooting a couple of trees. Interestingly, while a wall cloud was visible at this time, no funnel cloud was apparent. In fact, the first visual observation of a brief funnel cloud was at 2202 UTC (Fig. 2). As the tornado moved to the east-southeast (ESE), the funnel was observed to make continuous contact with the ground beginning at 2206 UTC, 14 min after tornadogenesis. These observations highlight the important fact that a tornado may be present and producing damage at the ground, but may not be associated with a visible funnel.

As the tornado continued to move eastward, it was intercepted by the Tornado Intercept Vehicle (TIV;

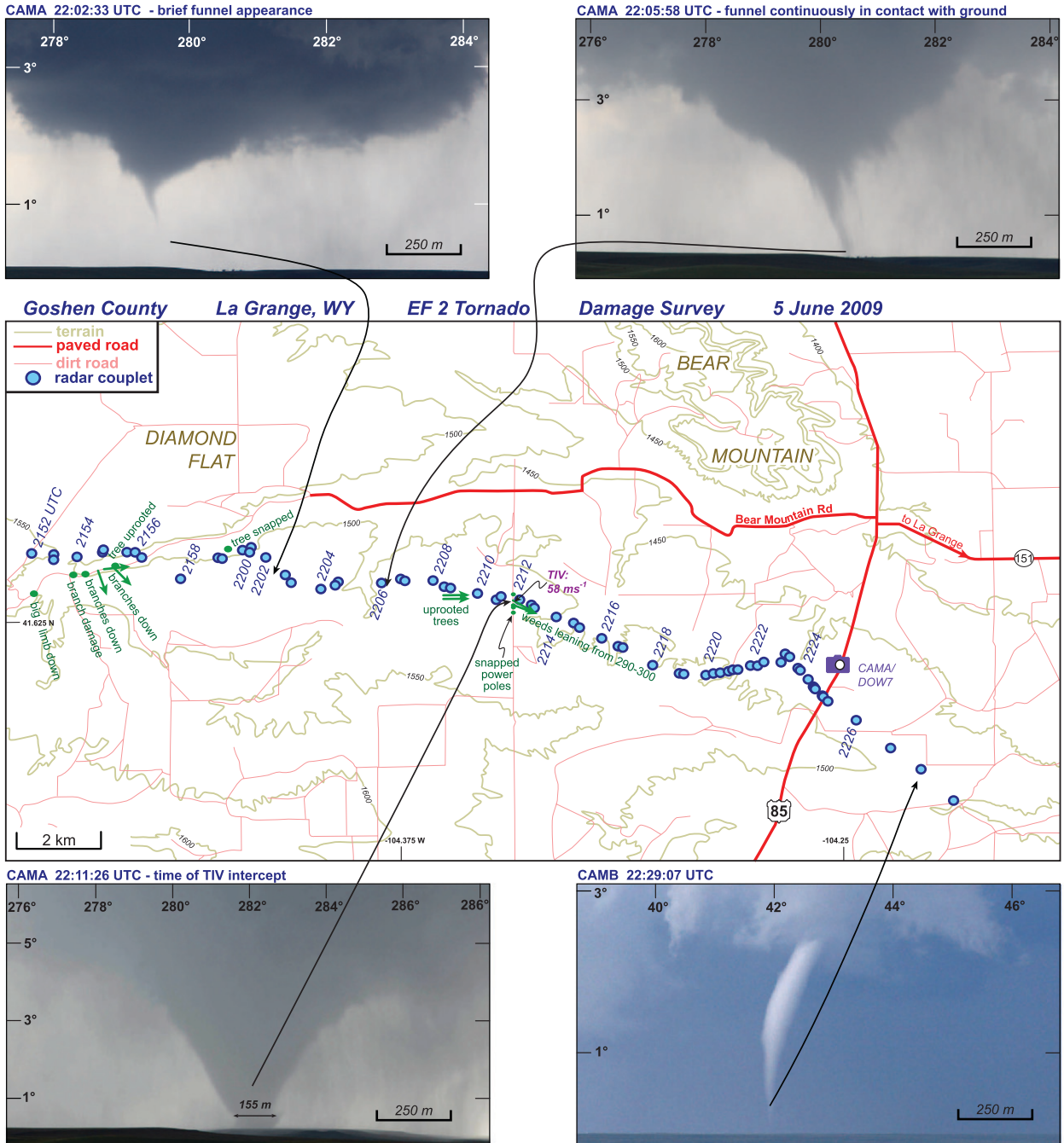


FIG. 2. Photographs at (top left) 2202:33, (top right) 2205:58, (bottom left) 2211:26, and (bottom right) 2229:07 UTC of the La-Grange tornado. All photos except for the one at 2229:07 UTC were taken at the CAMA/DOW 7 position shown in (middle). The 2229:07 UTC photo was taken at the CAMB/DOW 6 position located on Highway 85 southwest of the CAMA/DOW 7 location by about 15 km (not shown). The photos have been reduced or enlarged to ensure the azimuthal spatial distances are the same. (middle) The locations of damage (green) and the location of the radial velocity couplet (blue).

Wurman et al. 2007a) at about 2211 UTC. At this time, four power poles were snapped and the TIV recorded winds in the tornado of approximately 58 m s^{-1} (J. Wurman, K. Kosiba, and P. Robinson 2012, unpublished

manuscript). The snapped power poles and TIV in situ measurements were used by the National Weather Service to assign this tornado an EF 2 rating. The tornado continued to move to the ESE requiring the DOW

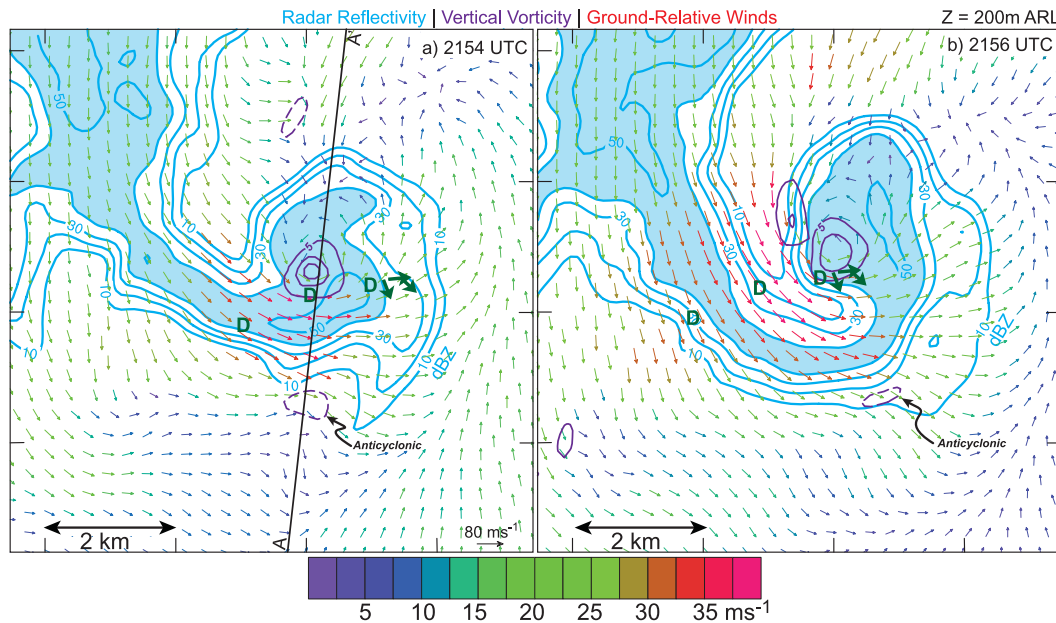


FIG. 3. Radar reflectivity (dBZ; blue), ground-relative winds (m s^{-1} ; color vectors), and vertical vorticity ($\times 10^{-2} \text{ s}^{-1}$; purple) at (a) 2154 and (b) 2156 UTC. The color bar on the bottom of the figure is for the ground-relative winds. Vertical vorticity is contoured every $5 \times 10^{-2} \text{ s}^{-1}$ with the zero line omitted for figure clarity. Solid and dashed vertical vorticity contours represent positive and negative values, respectively. All fields are at 200 m ARL. The thick green vectors and “D” symbols indicate locations and direction of damage indicators. The black line in (a) labeled A–A’ indicates the cross-sectional location shown in Fig. 4.

7 and CAMA teams to evacuate their deployment location at about 2218 UTC. The tornado then passed over Highway 85 just south of the DOW 7 deployment location. By 2229 UTC, the funnel diameter was roping out and dissipated shortly thereafter.

4. Combined dual-Doppler and photogrammetry analysis

a. Initial damage and vortex couplet

Shortly after tornadogenesis, the tornado produced minor damage. The location of this damage relative to the hook echo at 2154 and 2156 UTC is shown in Fig. 3. At this time, the tornado was moving to the ESE at about 12 m s^{-1} . Based on the location and direction of the damage indicators, it appears that the initial damage was produced by both the tornado and the rear-flank downdraft. The rear-flank downdraft was likely responsible for damaged trees and tree limbs far removed from the tornado or those that were down to the southeast. The tornado was responsible for damage indicators located on the southern flank of the vortex or those that were blown down to the east. Damage at later times (Fig. 2) was produced by the tornado as it was located on the southern flank of the circulation. The overall amount of damage

produced by this tornado was minimal, as confirmed by a detailed aerial damage survey. The paucity of damage is not surprising since much of the terrain over which the tornado traveled was ranchland.

Another feature resolved in the dual-Doppler analysis shown in Fig. 3 is the vertical vorticity couplet. The tornado and low-level mesocyclone were located in the high-reflectivity region of the hook while a weaker anticyclonic circulation, evident in the vertical vorticity field, was located on the southern edge of the high-reflectivity region. Vertical vorticity couplets straddling the hook echo have long been observed and documented in the literature (e.g., Brandes 1977, 1978, 1981, 1984; Fujita and Wakimoto 1982; Wakimoto and Liu 1998; Wakimoto et al. 1998; Wakimoto and Cai 2000; Wurman and Gill 2000; Bluestein and Gaddy 2001; Markowski et al. 2008). Markowski et al. (2008) examined the distribution and orientation of vortex lines within the hook region for a number of supercells observed during the first VORTEX field program (Rasmussen et al. 1994) that contained vortex couplets. The vortex lines formed arches directed upward from the cyclonic circulation passing over the high-reflectivity region of the hook and downward into the anticyclonic circulation. The implication of this vortex line distribution was that solenoidally generated horizontal vorticity across the rear flank gust front was being

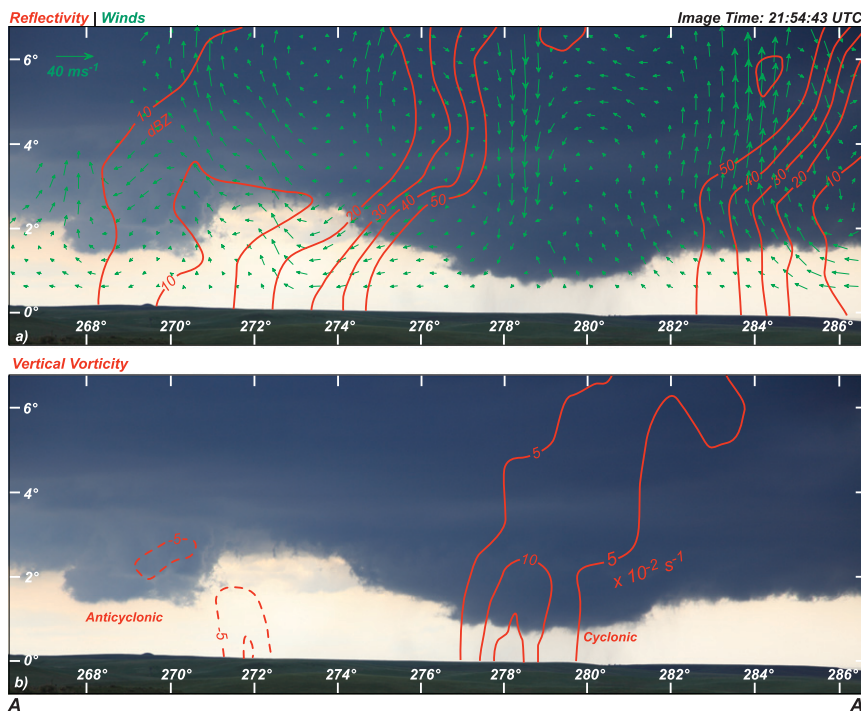


FIG. 4. Vertical cross section of radar data (2154:07–2154:57 UTC) through the cyclonic vertical vorticity maximum along A–A' shown in Fig. 3a superimposed on a photograph taken at 2154:43 UTC. (a) Radar reflectivity (dBZ) is contoured in red and winds ($m s^{-1}$) in the plane of the cross section are plotted as green vectors. (b) Vertical vorticity is contoured in red every $5 \times 10^{-2} s^{-1}$ with the zero line omitted for figure clarity. Solid and dashed contours are positive and negative values, respectively.

tilted upward by the storm's updraft, producing the vortex pair. Consistent with Markowski et al. (2008), Markowski et al. (2011b) documented vortex line arches during the pretornadic phase of the Goshen County supercell.

The existence of two lowered cloud bases was observed in a photo taken at 2154:43 UTC (Fig. 4). The primary cyclonic lowering was located between azimuths 275° – 282° . Consistent with Fig. 3, it was embedded in high reflectivity and associated with a downdraft at or above the cloud base (Fig. 4a). The circulation was strongest near the surface, as illustrated in the vertical vorticity field (Fig. 4b). The second lowering was located between azimuths 267° – 271° (Fig. 4b). It was collocated with the local minimum of vertical vorticity south of the hook in Fig. 3a.

b. Evolution of tornado and mesocyclone intensities

An important question that has received little attention in the literature is “how well does the intensity of the low-level mesocyclone correlate with those of the tornado and attendant surface damage?” Because of the tornado’s relatively small spatial scale, the current network of Weather Surveillance Radar–1988 Doppler (WSR-88D) do not resolve the tornadic circulation unless it is at close range to the radar and relatively large

in size (Wood et al. 2009). The WSR-88Ds will, however, sometimes resolve the low-level mesocyclone as it is often an order of magnitude wider. Thus, if the intensities of the low-level mesocyclone and tornado are well correlated, it would be possible to monitor tornado intensity changes in real time. Burgess et al. (2002) addressed this issue by analyzing DOW and WSR-88D data collected on the 3 May 1999 F5 Oklahoma City tornado. Trends in DOW radial velocity data of the tornadic circulation were well correlated to surface wind damage intensity. However, the same was not true for WSR-88D observations of the tornado cyclone. In another study, Wakimoto et al. (2003) showed with airborne Doppler radar data that no definitive relationship existed between the intensity and sizes of a low-level mesocyclone and the F5 tornado it spawned.

The 5 June 2009 photography and dual-Doppler data were examined to address this question. In the subsequent analyses, the funnel diameter was assumed to be directly proportional to tornado intensity since a detailed (enhanced Fujita) EF-scale analysis based on damage was not possible in this case. This assumption was tested by comparing the funnel diameter to the DOW 7 single-Doppler velocity difference across the tornado couplet at

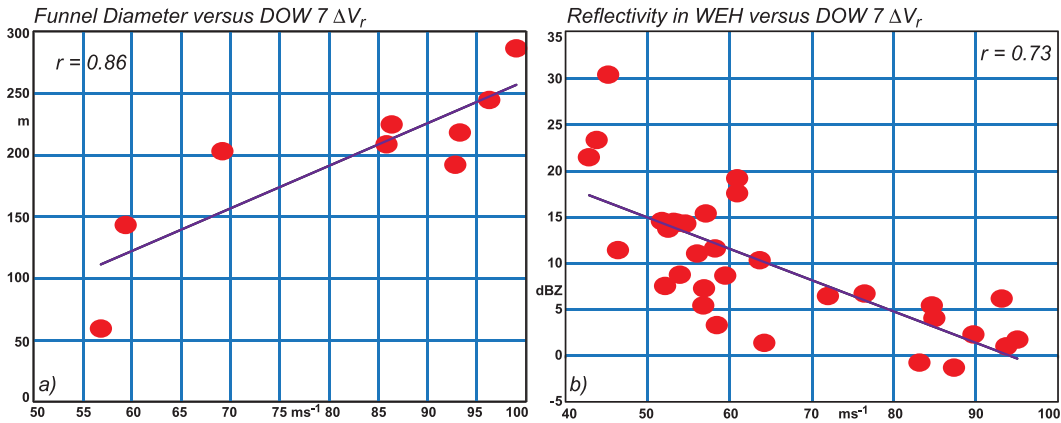


FIG. 5. Scatterplots of (a) funnel diameter (m) and (b) minimum DOW 7 reflectivity (dBZ) in the weak echo hole vs DOW 7 single-Doppler radial velocity difference (m s^{-1}) across the couplet.

times when the funnel was making contact with the ground and close enough to DOW 7 to sufficiently resolve the tornadic circulation (Fig. 5a). While it is acknowledged that the number of observations for this analysis is small, funnel diameter appears to be well correlated to tornado intensity. Maximum vertical vorticity and circulation, calculated from the dual-Doppler data, approximated mesocyclone strength. The tornado funnel diameter and vertical extent were estimated from photos taken during the dual-Doppler analysis times and were superimposed on the time–height diagram of maximum vertical vorticity associated with the mesocyclone (Fig. 6). At the time of tornadogenesis, the mesocyclone maximum

vertical vorticity was increasing at low levels. It continued to do so until about 2154 UTC when the first tree damage was observed (Figs. 2 and 6). Thereafter, the mesocyclone weakened slightly and then intensified dramatically at low levels through 2202 UTC. This evolution is consistent with Fig. 3 in Part I who showed the time evolution of the radial velocity couplet strength from DOW 7. Note that 2202 UTC was also the time that a brief, narrow funnel was observed to descend from cloud base, but did not reach the ground (Figs. 2 and 6). From 2202 to 2206 UTC, the mesocyclone intensity weakened at low levels. Just before 2206 UTC, however, the funnel reformed and began to make continuous contact with the ground. From 2206

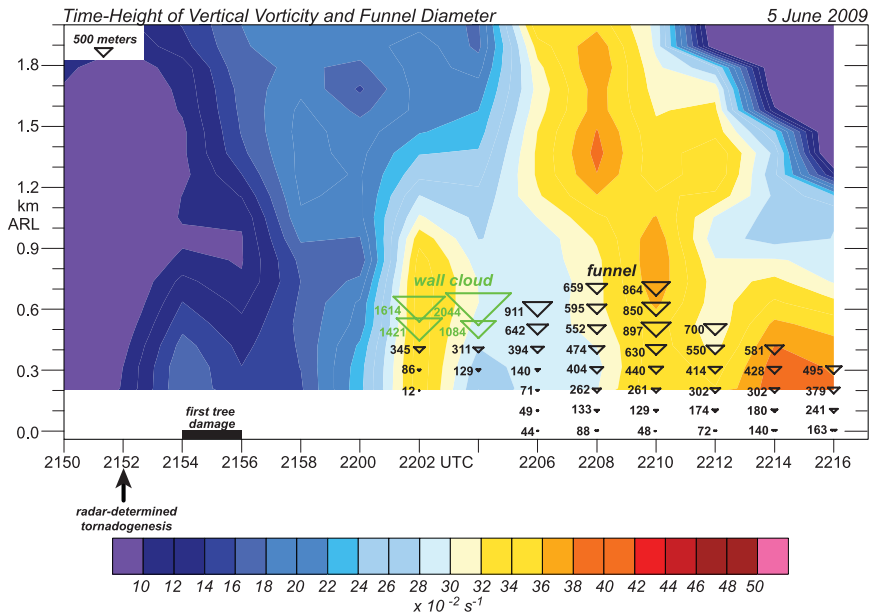


FIG. 6. Time–height plot of maximum vertical vorticity observed in the dual-Doppler data. Superimposed numbers and symbols represent the diameter (m) of the wall cloud (green) and funnel cloud (black) derived from the photogrammetric analysis.

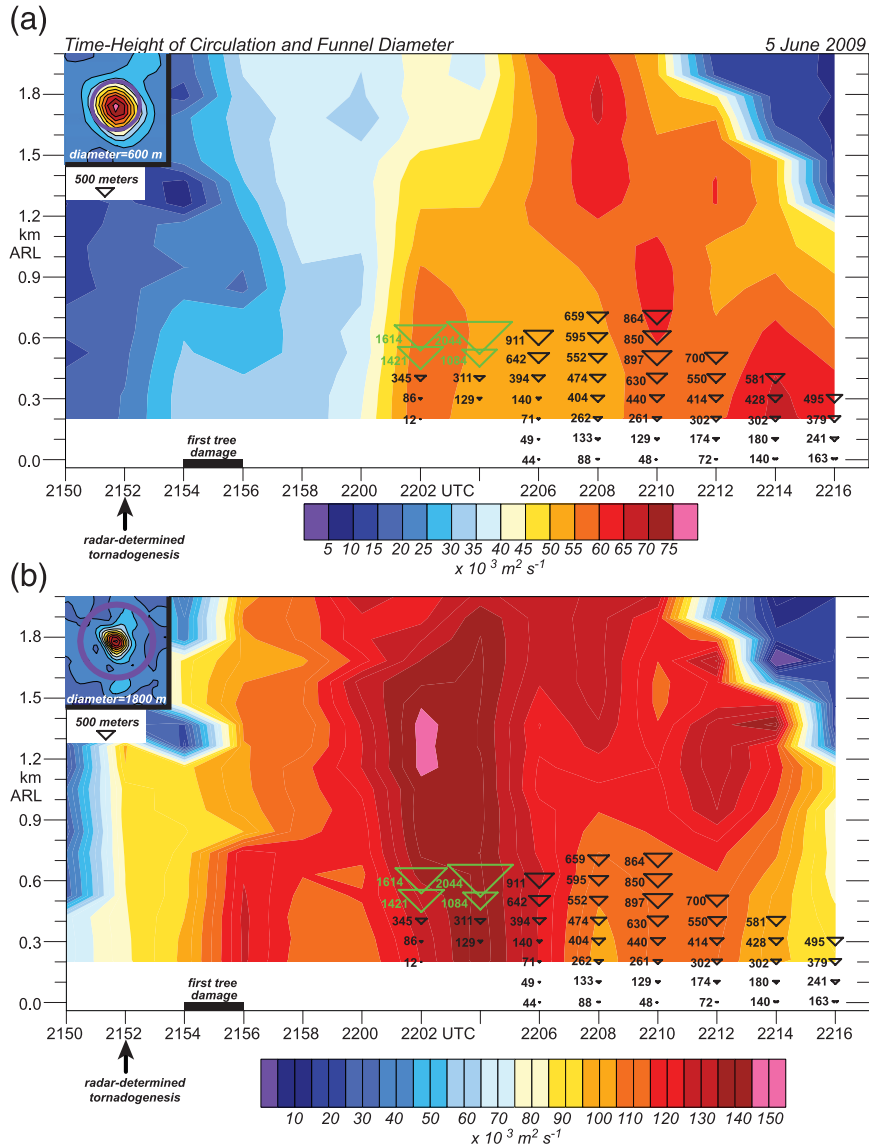


FIG. 7. Time–height plot of circulation ($\times 10^3 \text{ m}^2 \text{ s}^{-1}$) calculated from the dual-Doppler data over the area of a circle with diameter of (a) 600 and (b) 1800 m centered on the vertical vorticity maximum as shown in the inset diagrams. Superimposed numbers and symbols are as in Fig. 6.

to 2208 UTC, the funnel became wider from the surface to 400 m above radar level (ARL) whereas the mesocyclone intensity remained unchanged. After 2208 UTC, the funnel diameter became larger with time at nearly all levels. The low-level mesocyclone intensity increased to a maximum intensity of about $40 \times 10^{-2} \text{ s}^{-1}$ at about 2215 UTC. The near-surface funnel diameter increased through 2216 UTC. The results in Fig. 6 suggest that the tornado and mesocyclone intensities were not well correlated ($r = 0.24$).

A similar analysis was performed using circulation to estimate mesocyclone strength. Results are shown for

circulation calculated over the area of a circle with a diameter of 600 (Fig. 7a) and 1800 m (Fig. 7b) centered on the vertical vorticity maximum at each level. The evolution of circulation in Fig. 7a is similar to that shown for maximum vertical vorticity in Fig. 6 and again suggests that the mesocyclone intensity on smaller scales was not well correlated to the tornado intensity ($r = 0.21$). The larger-scale circulation evolution, however, is much different (Fig. 7b). There was a dramatic increase in low-level circulation from 2154–2156 UTC when the first tree damage was observed. A second intensification began at about 2202 UTC with the largest values of circulation

($150 \times 10^3 \text{ m}^2 \text{ s}^{-1}$) observed at 1.2–1.5 km ARL. This is also the time that a well-defined wall cloud and pendant funnel was briefly observed (Fig. 2). As the funnel formed and made contact with the ground at 2206 UTC, circulation within the mesocyclone began to weaken. Thereafter, as the low-level funnel diameter increased, the mesocyclone circulation below 1 km ARL decreased.

Another representation of circulation evolution is shown in Fig. 8 where circulation at 200 m ARL is plotted as a function of diameter for all dual-Doppler times from 2158 to 2216 UTC. At small diameters (less than approximately 800 m), circulation generally increased with time from 2158 to 2216 UTC (Fig. 8b) and linearly increased with diameter. This is consistent with the funnel diameter generally becoming larger over the same period of time. These data, therefore, suggest that there is some signal of the tornadic circulation in the dual-Doppler analysis on these small spatial scales. In other words, the circulation observed at diameters less than 800 m was influenced by the tornado. Perhaps this is not surprising since the response function associated with the two-pass Barnes scheme used in the dual-Doppler analysis does not completely eliminate all wave energy until the wavelength is less than about 300 m.

Circulation evolution of the mesocyclone at larger diameters (greater than about 1200 m) was much different. Initially, circulation increased with time from 2158 to about 2206 UTC. Recall that this is the time the funnel was first observed to make contact with the ground. Thereafter, circulation within the larger-scale mesocyclone began to decrease even though circulation closer to the tornado was increasing, along with the funnel diameter. By 2216 UTC, the magnitude of circulation was relatively constant at diameters greater than 800 m. Interestingly, the funnel diameter was widest at 2218 UTC and began to dissipate thereafter. This may not be surprising since the circulation at diameters greater than 1200 m prominently decreased after 2212 UTC. The results in Figs. 6–8 highlight the complex relationship between the tornado and low-level mesocyclone.

c. Evolution of the weak echo hole and mesocyclone

WEHs are often observed within hook echoes and are commonly associated with tornadoes (Fujita 1981; Wurman et al. 1996; Wakimoto et al. 1996; Wurman and Gill 2000; Bluestein et al. 2004, 2007b; Wurman et al. 2010). The WEH appears within the tornado core (Davies-Jones et al. 2001) and is likely created by the centrifuging of hydrometeors and debris (Dowell et al. 2005). Therefore, as the tornadic circulation strengthens, one would expect the reflectivity values within the WEH to decrease except near the ground where lofted debris may contribute scatterers near the center of the tornado.

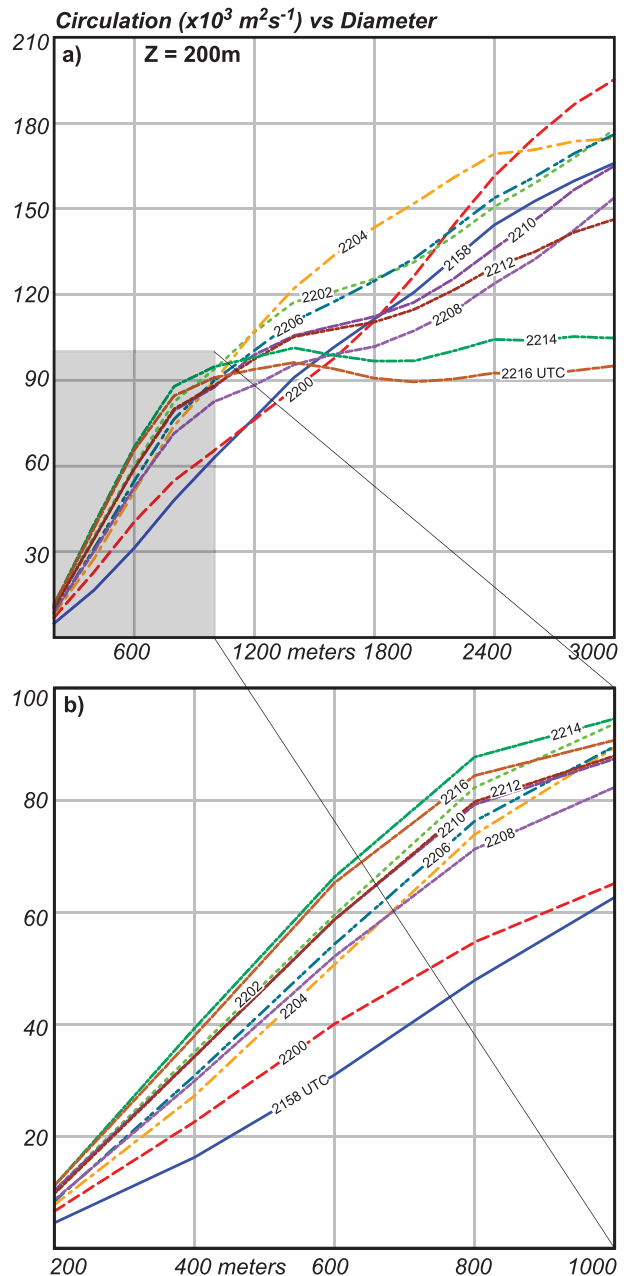


FIG. 8. (a) Plots of circulation ($\times 10^3 \text{ m}^2 \text{ s}^{-1}$) vs diameter for dual-Doppler times ranging from 2158–2216 UTC, every 2 min. (b) Data in the gray shaded area in (a) are shown. All data were calculated at a height of 200 m.

This assumption was tested by comparing the minimum reflectivity within the WEH with the concurrent DOW 7 radial velocity difference across the couplet. This relationship is shown in Fig. 5b and suggests that the WEH minimum reflectivity is anticorrelated with the couplet strength.

The relationship between the minimum reflectivity value in the WEH and the maximum vertical vorticity of

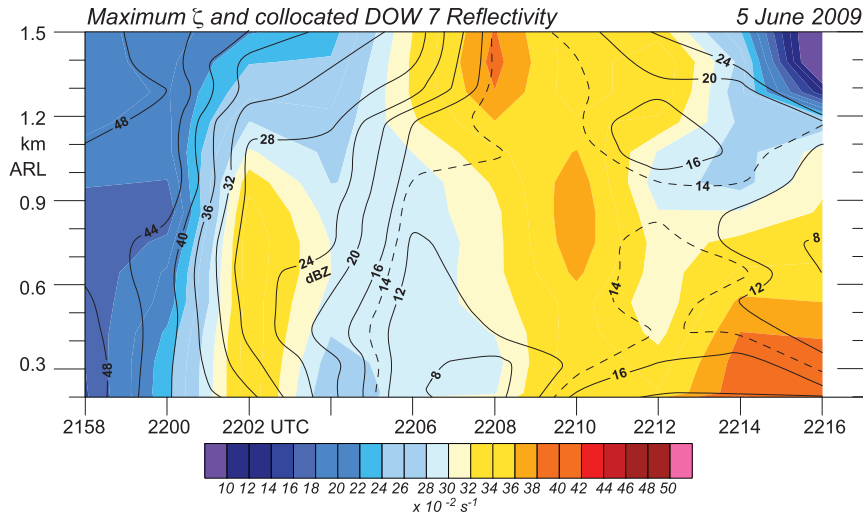


FIG. 9. Time–height plot of maximum vertical vorticity associated with the primary cyclonic circulation in the dual-Doppler domain. Black contours are DOW 7 radar reflectivity values at the same location as the vertical vorticity maximum.

the mesocyclone is shown in Fig. 9. As the mesocyclone strengthened from 2158–2202 UTC, the reflectivity values weakened to less than 40 dBZ, the value used to define the WEH in Part I. From 2202 to 2206 UTC, the WEH reflectivity values continued to decrease suggesting that the tornadic circulation, which was not yet visible (Figs. 6 and 7), was strengthening. During this same period of time, the maximum vertical vorticity associated with the mesocyclone either remained unchanged or weakened.

This result provides more evidence that intensity changes in the mesocyclone do not lead to changes in tornado intensity. By 2208 UTC, the reflectivity values in the WEH were about 8 dBZ. This was also the time when the mesocyclone maximum vertical vorticity was a local minimum. After 2208 UTC, the WEH reflectivity values increased as did the strength of the mesocyclone.

An alternative representation of the data in Fig. 9 is shown in Fig. 10 where a scatterplot of DOW 6 and 7

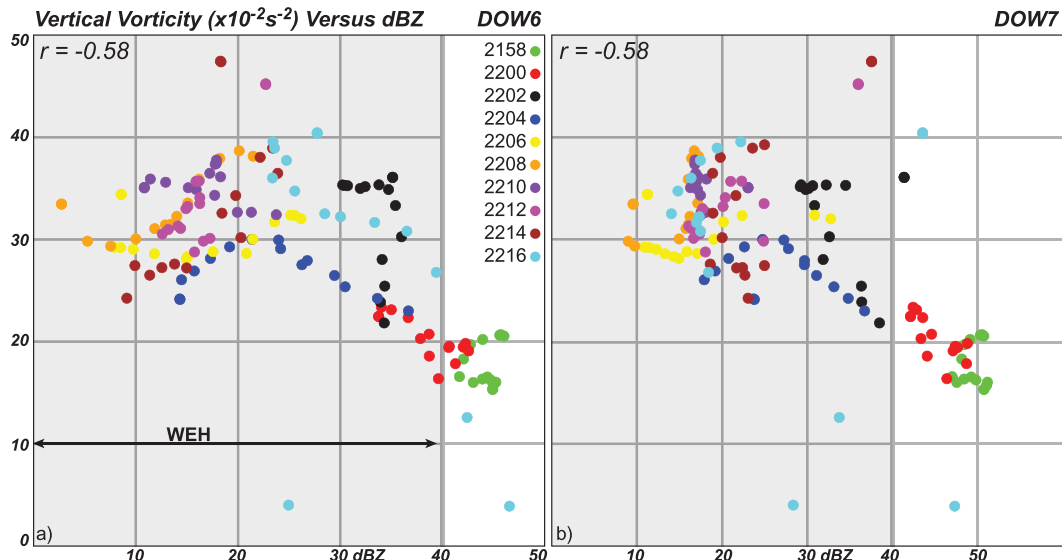


FIG. 10. Scatterplot of (a) DOW 6 and (b) DOW 7 reflectivity (dBZ) values at the location of maximum vertical vorticity in the dual-Doppler domain at grid altitudes ranging from 0.2 to 1.5 km AGL. Data points are color coded according to the time of observation (in UTC), as shown in the legend in (a). The shaded area represents reflectivity values less than 40 dBZ.

reflectivity versus maximum vertical vorticity are plotted and color coded according to observation time. As the mesocyclone strengthened from 2158 to 2202 UTC, the reflectivity values in the WEH linearly decreased (Fig. 10). At later times, significant scatter is apparent in the data ($r = -0.58$) suggesting a weak relationship between the intensities of the tornado and mesocyclone. Some of the scatter in the data at later times may be attributed to the tornado lofting debris at low levels. Removing all data in the lowest 200 m (not shown) results in improved correlations with $r = -0.63$ and -0.75 for DOW 6 and 7, respectively.

d. Location of the hook echo, WEH, and tornado funnel

The dataset presented herein provide a unique opportunity to examine the relative spatial scales of the hook echo, WEH, vertical vorticity, and funnel cloud. Results of this analysis are shown in Fig. 11. The radar reflectivity data of the hook and WEH in Fig. 11b have been rotated clockwise 90° to facilitate the comparison. The spatial scale of the hook echo in Fig. 11b is about 5.3 km, measured from the southern edge of the high-reflectivity region south of the WEH, to the main precipitation region of the storm. The WEH (<40 dBZ) has a diameter of approximately 0.85 km. The purple contour in Fig. 11b is the $5 \times 10^{-2} \text{ s}^{-1}$ vertical vorticity isopleth, shown in Fig. 11c. The diameter of the $5 \times 10^{-2} \text{ s}^{-1}$ vertical vorticity isopleth is approximately 0.8 km, similar to the WEH. The profile of vertical vorticity contours in Fig. 11c is plotted on the photo in Fig. 11a. The spatial scales in these two panels are identical. Clearly, the funnel is well within the WEH. The funnel diameter at the cloud base and at the surface is about 0.6 and 0.09 km, respectively. Therefore, the surface funnel diameter is about 11% and 1.7% of the WEH and hook echo scales, respectively.

e. Vertical vorticity and vertical velocity

The wind field and intensity of the mesocyclone relative to the funnel are now examined in Fig. 12. Vertical cross sections of the vertical vorticity and winds were superimposed on photos of the tornado. Beginning with the photo taken at 2205:58 UTC (Fig. 12a), the mesocyclone horizontal extent did not vary appreciably with height, inferred by the near-vertical isopleths of vertical vorticity and location of the radius of maximum wind (RMW). At the same time, the tornado funnel tapered to much smaller diameters near the ground. Also apparent at 2205:58 UTC is that the mesocyclone exhibited two local maxima in vertical vorticity: one near the ground and the other above the cloud base. This was also observed at

2208:30 (Fig. 12b) and 2212:03 UTC (Fig. 12d) and is consistent with the double-couplet structure documented by Part I. The wind field at 2205:58 UTC in the plane of the photo and inset vertical velocities showed that the tornado was located on a gradient of vertical motion. At 2208:30 UTC, the spatial extent and intensity of the mesocyclone had not changed appreciably. While the tornado was located on a gradient of vertical velocity, the locations of updraft and downdraft had reversed since 2205:58 UTC. Furthermore, the funnel had widened noticeably at elevation angles less than 2° suggesting an intensification of the low-level tornadic circulation. A significantly tapered funnel was observed at 2209:58 UTC. Similar to 2208:30 UTC, the funnel was located on a gradient of vertical motion. By 2212:03 UTC, the mesocyclone had intensified at low levels with vertical vorticity values exceeding $40 \times 10^{-2} \text{ s}^{-1}$. Vertical velocities at 700 m ARL were relatively weak. Over the next few minutes (Figs. 12e,f), the low-level funnel continued to widen with time. Within the mesocyclone, significant axial downdraft developed aloft but had not reached the ground.

f. Angular momentum

The distribution and evolution of angular momentum in the hook echo is of particular interest as conservation of this quantity within the swirling inflow may play a role in the genesis and maintenance of tornadoes (e.g., Lee and Wurman 2005; Rasmussen and Straka 2007; Kosiba and Wurman 2010). Azimuthally averaged angular momentum was computed and superimposed on select photos in Fig. 13. At 2158:21 UTC (Fig. 13a), angular momentum increased radially outward below the cloud base indicating that high angular momentum air at low levels was present within the mesocyclone. Recall that 2158:21 UTC was about 6 min after tornadogenesis and 8 min before the funnel made continuous contact with the ground. At and above the cloud base, the radial increase of angular momentum terminated just beyond the cyclonic cloud-base lowering. This is also evident at 2205:58 and 2212:03 UTC (Figs. 13b,c). These observations are consistent with those of Rasmussen and Straka (2007) who examined the distribution of angular momentum and budget relative to the wall cloud and tornado observed near Dimmitt, Texas, on 2 June 1995.

Consistent with the circulation evolution shown in Fig. 7b, angular momentum within the low-level mesocyclone increased from 2158:21 to 2205:58 UTC (Figs. 13a,b and 14a). This increase was observed out to radii of at least 1.7 km from the circulation center (Fig. 14a). Recall that the tornado was also strengthening during this period of time. Yet, the low-level azimuthally averaged secondary circulation at 2158:21 and 2205:58 UTC was divergent, or downward and outward, transporting low

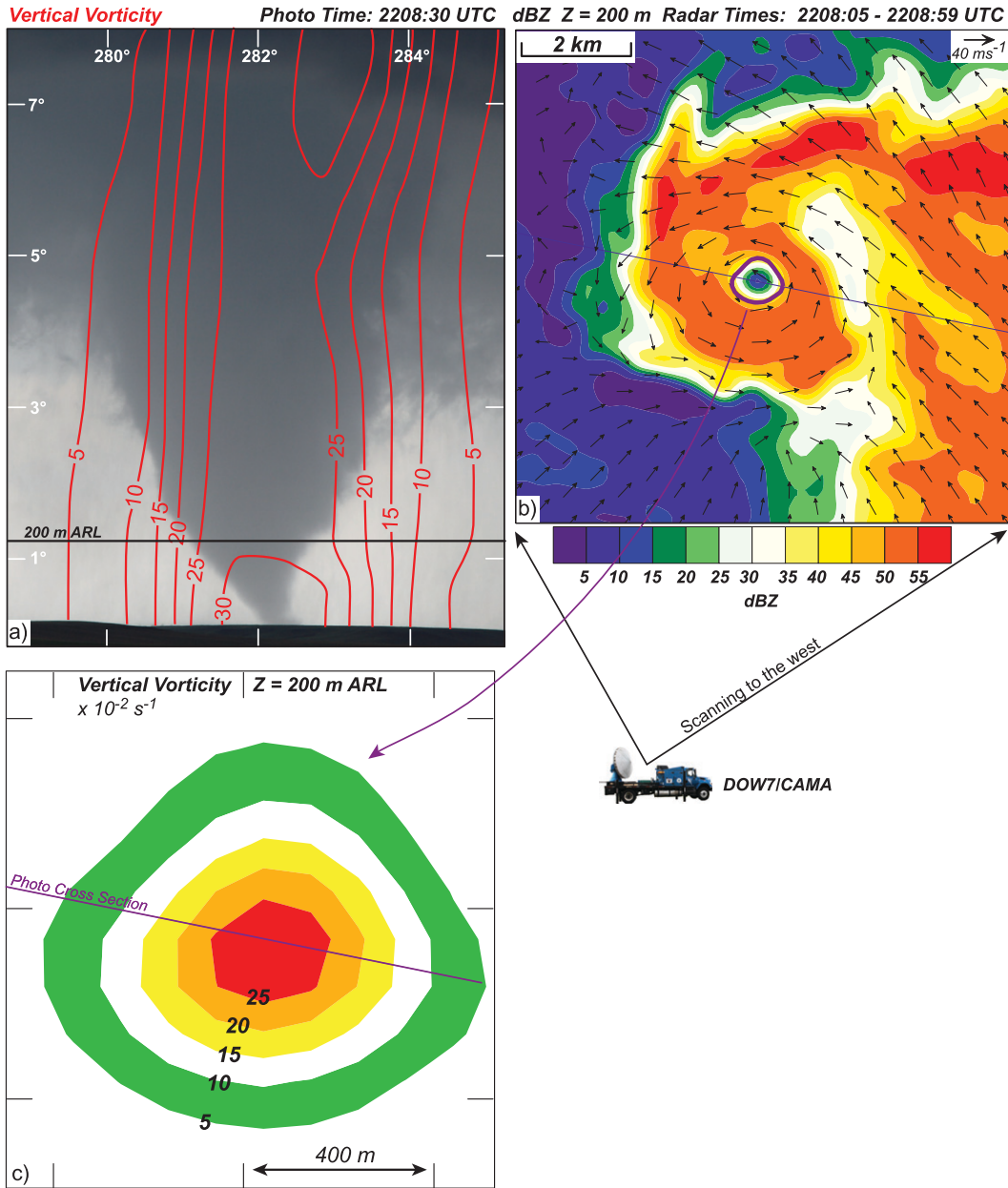


FIG. 11. (a) Photograph taken at 2208:30 UTC with superimposed vertical vorticity ($\times 10^{-2} \text{ s}^{-1}$; red). The location of 200 m ARL is shown with the horizontal black line and indicates the location of the plan view cross sections shown in (b) and (c). The radar data cross-sectional location is shown in (b) and has the same orientation as the photograph. (b) Plan view at 200 m ARL of DOW 7 radar reflectivity (dBS; color) and storm-relative winds (m s^{-1} ; black vectors). The thick purple contour is the $5 \times 10^{-2} \text{ s}^{-1}$ vertical vorticity value. (c) Plan view of vertical vorticity ($\times 10^{-2} \text{ s}^{-1}$) centered on the primary cyclonic circulation at 200 m ARL.

angular momentum air away from the circulation center. Rasmussen and Straka (2007) and Markowski et al. (2011a) observed similar secondary circulations within tornadic low-level mesocyclones, but during the transition or weakening phases of the low-level mesocyclone. Given that the angular momentum tendency was positive from 2158:21 to 2205:58 UTC, it is possible that eddy flux

convergence of angular momentum was large enough to overcome the loss by outward advection as was observed by Rasmussen and Straka (2007) during the transition phase of the 2 June 1995 Dimmitt, Texas, tornado cyclone. After 2205:58 UTC (Figs. 13c,d and 14b,c), the angular momentum distribution associated with the mesocyclone underwent a dramatic change. At 2212:03 UTC (Fig. 13c)

5 June 2009

Vertical Vorticity

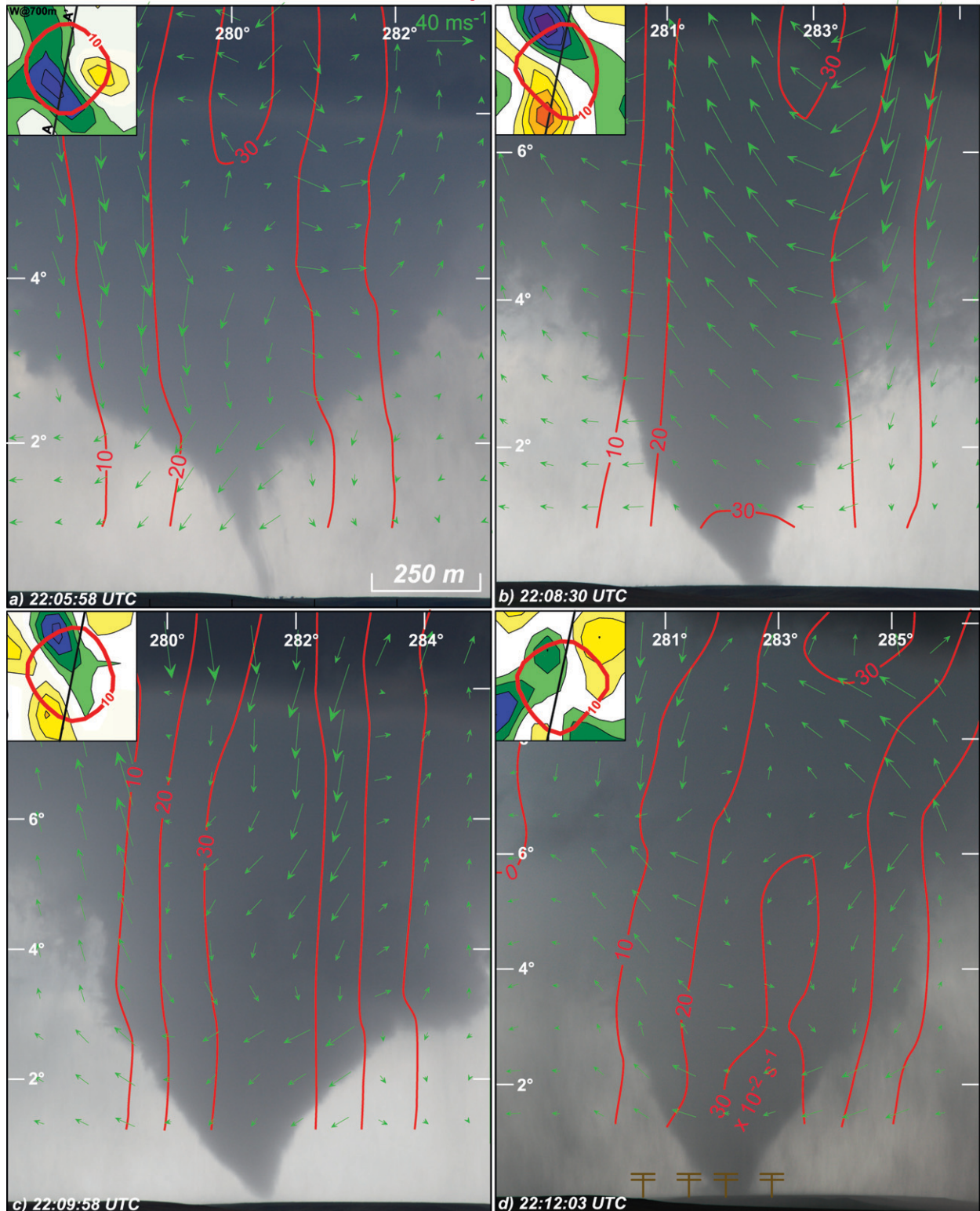


FIG. 12. Photographs taken at (a) 2205:58, (b) 2208:30, (c) 2209:58, (d) 2212:03, (e) 2214:01, and (f) 2216:23 UTC. Winds (m s^{-1}) in the plane of the cross section are shown in the green vector field. Vertical vorticity ($\times 10^{-2} \text{ s}^{-1}$) is contoured in red. Locations of damaged telephone poles in Fig. 2 are shown in (d). The inset fields show vertical velocity (color scale at bottom of figure) and the $10 \times 10^{-2} \text{ s}^{-1}$ vertical vorticity contour in red. All inset fields are at 700 m ARL. The location of the radar vertical cross section is shown as the black line labeled A–A' in the inset diagrams. The position of this cross section at 700 m AGL is shown as the black horizontal line in (a)–(f).

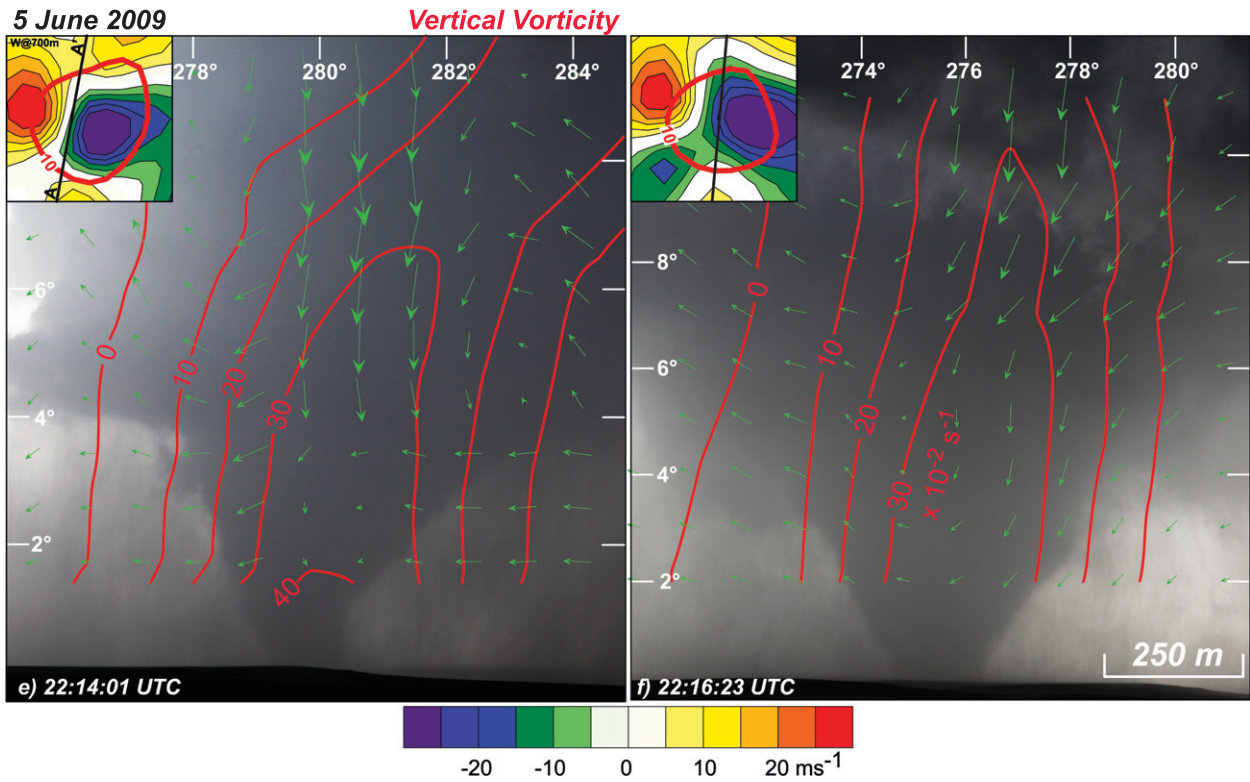


FIG. 12. (Continued)

and 2216:23 UTC (Fig. 13d), the radial gradient of angular momentum decreased dramatically. This change is largely due to the decreased magnitude of the low-level maximum observed at large diameters. The angular momentum tendency from 2212:03–2205:58 UTC was negative at low-level radii beyond 0.5 km (Fig. 14b). This difference was even larger between 2216:23 and 2212:03 UTC suggesting an acceleration of the low-level mesocyclone demise. The weakening angular momentum after 2206 UTC is consistent with the decreasing strength of circulation shown in Fig. 7b and may be attributed to the downward and outward secondary circulation. Interestingly, during this same period of time, the tornado funnel diameter was increasing and reached its largest extent at about 2218 UTC, consistent with the single-Doppler azimuthal shear evolution shown in Fig. 3 in Part I. The positive values of angular momentum change near the circulation center in Fig. 14 may be a reflection of the intensifying tornado.

Another presentation of angular momentum evolution at 200 m is shown in the time–diameter plot in Fig. 15. From 2150 to 2204 UTC, angular momentum at most all radii increased. This result is consistent with the interpretation of the data shown in Figs. 13a,b and 14a. After 2204 UTC, angular momentum at most all radii either remained constant or weakened. The observations

in Figs. 13–15 provide more evidence that the visual tornado evolution evolved independently from the parent mesocyclone.

5. Summary and conclusions

This is the second of a two-part study that has presented results of the synthesis of high-resolution radar observations, cloud photography, and damage survey data of the 5 June 2009 Goshen County tornado that was observed during the Second Verification of the Origins of Rotation in Tornadoes Experiment (VORTEX2). In Part I, single-Doppler radar data from DOW 7 were merged with photos of visual features within the hook region, including the tornado funnel. In Part II, dual-Doppler data derived from DOW 6 and 7 were integrated with the photography data. The primary objective of Part II was to examine the relationship between the visual characteristics of the wall cloud and tornado with the kinematic evolution of the mesocyclone that was resolved in the dual-Doppler analysis. Radar and photography data were collected from well before tornadogenesis through the demise of the visual funnel. Ground and aerial damage surveys were performed after the event. The surveys uncovered only minimal damage to trees and four downed telephone poles. This data along with in situ data from the Tornado

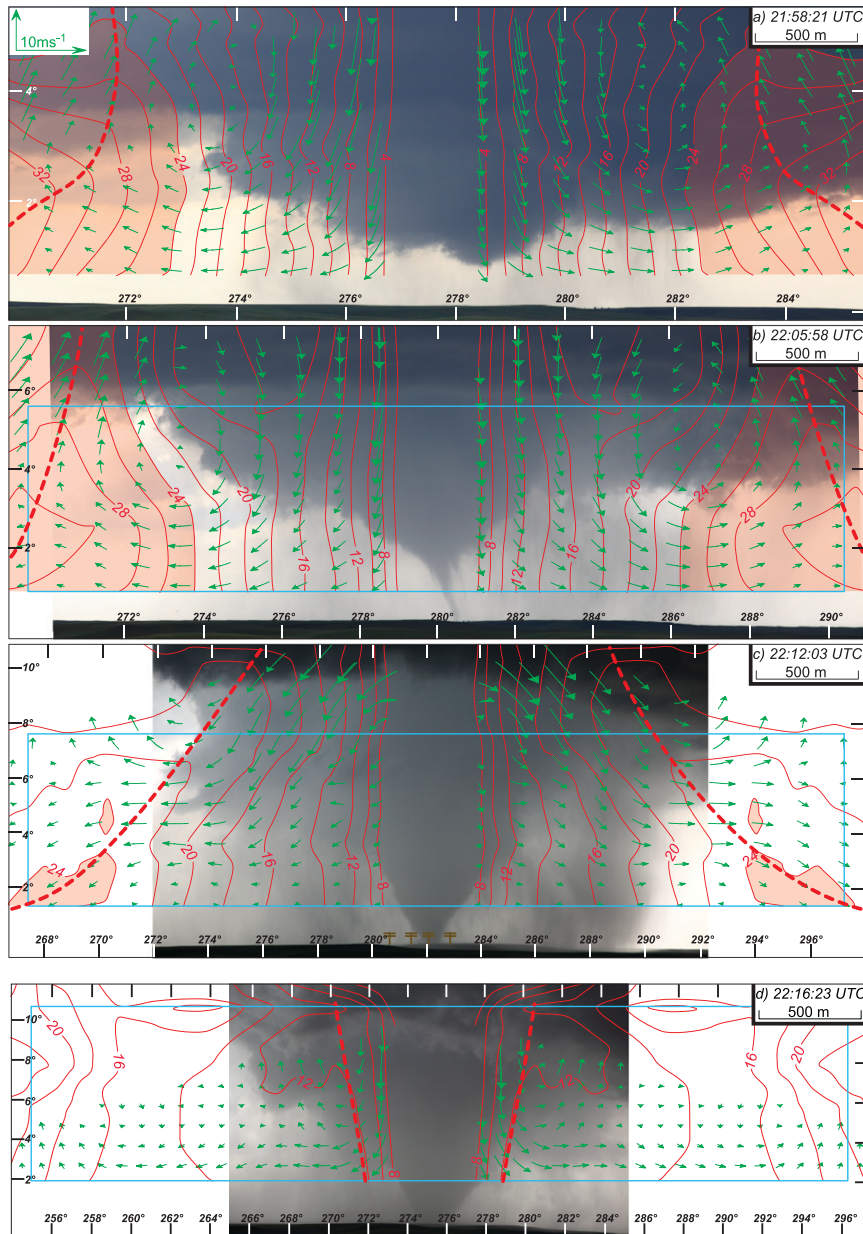


FIG. 13. Photographs taken at (a) 2158:21, (b) 2205:58, (c) 2212:03, and (d) 2216:23 UTC with superimposed azimuthal average angular momentum ($\times 10^3 \text{ m}^2 \text{ s}^{-1}$; red) and winds in the plane of the cross section (m s^{-1} ; green) derived from the dual-Doppler data. Angular momentum values greater than $24 \times 10^3 \text{ m}^2 \text{ s}^{-1}$ are shaded. Solid and dashed radial velocity contours represent flow away and toward the circulation center, respectively. The thick red dashed line approximately delineates the radius where angular momentum no longer radially increases. Blue boxes are the approximate data locations shown in Fig. 14.

Intercept Vehicle led to an EF 2 intensity rating by the National Weather Service. A summary of the primary findings of this study follows.

Tornadogenesis and initial tree damage occurred 14 min before the funnel was observed to make continuous contact with the ground. This observation highlights

the important conclusion that damaging tornadic circulations may not always be visible. While a cyclonic cloud base lowering was observed well before and during the time the tornado was visually apparent, a separate anticyclonic lowering was briefly observed shortly after tornadogenesis south of the cyclonic wall cloud.

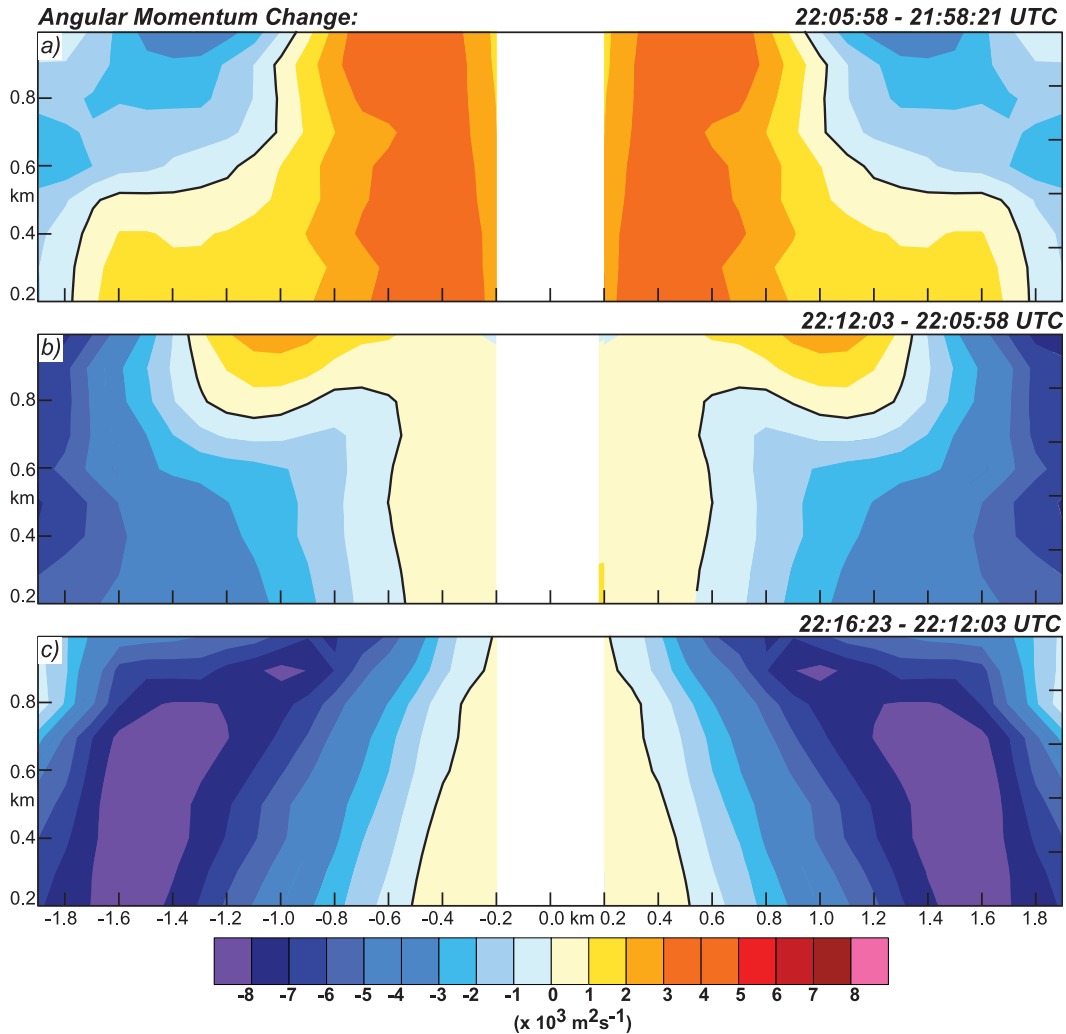


FIG. 14. Change in angular momentum ($\times 10^3 \text{ m}^2 \text{ s}^{-1}$) from (a) 2205:58–2158:21, (b) 2212:03–2205:58, and (c) 2216:23–2212:03 UTC. The thick black contour is the zero line. The approximate data locations in (a)–(c) are shown as the light blue boxes in Figs. 13b–d.

A number of analyses were presented that examined how well tornado intensity was correlated to the strength of the mesocyclone. Mesocyclone strength was estimated by computing maximum vertical vorticity and circulation from the dual-Doppler data. Given the dearth of damage over the tornado path, other variables in addition to single-Doppler radial velocities were used to estimate tornado strength. The first was funnel diameter, which was well correlated to the DOW 7 radial velocity difference observed within the tornado couplet. It was shown that funnel diameter was not well correlated with mesocyclone intensity. From the time of tornadogenesis until the funnel was observed continuously on the ground (a total of about 14 min), the tornado and low-level mesocyclone intensities both generally increased. Thereafter, the funnel diameter slowly became wider

for the next 12 min as the tornado intensified. However, circulation computed over a large portion of the low-level mesocyclone and maximum vertical vorticity decreased. Consistent with the single-Doppler azimuthal shear evolution shown in Part I, during the period of time when the tornadic circulation was strengthening, circulation calculated over a small area (circle with diameter equal to 600 m) increased. This observation was attributed to the fact that not all of the tornado circulation was filtered out of the dual-Doppler analysis.

Another measure of tornado intensity was the minimum reflectivity observed within the WEH (Dowell et al. 2005). As the tornadic winds strengthen, more hydrometeors are centrifuged from the center of the circulation, lowering the reflectivity values within the WEH. Scatterplots

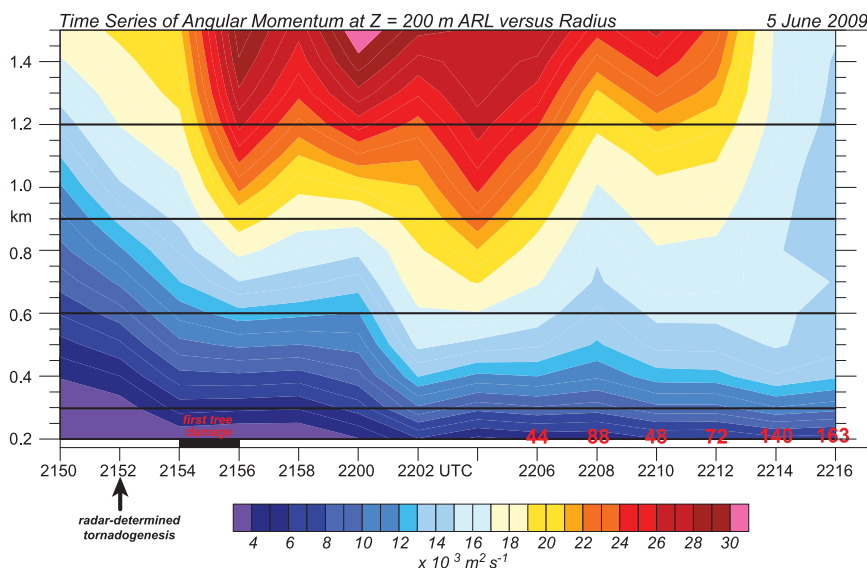


FIG. 15. Time–radius plot of azimuthal average angular momentum ($\times 10^3 \text{ m}^2 \text{ s}^{-1}$) computed at 200 m ARL. Red numbers indicate the funnel cloud diameter (m) at 100 m ARL at the respective times.

of maximum vertical vorticity versus reflectivity within the WEH for times when the WEH was observed showed weak negative correlation between the two fields ($r = -0.58$) with larger maximum vertical vorticity values generally associated with smaller reflectivities. These results have important operational implications since the current network of WSR-88Ds can only detect the mesocyclone owing to the azimuthal resolution of the radar beam. This study suggests that it may not be possible to infer tornado intensity based on the strength and evolution of the mesocyclone.

The distribution and evolution of angular momentum were also examined. Azimuthally averaged angular momentum increased radially outward from the circulation center and became relatively constant with increasing radius at or just beyond the wall cloud edge. From the time of tornadogenesis until the funnel was observed continuously on the ground, azimuthally averaged angular momentum increased in the intensifying mesocyclone. At the same time, however, the low-level azimuthally averaged wind field was divergent, transporting low angular momentum air away from the circulation center. It is hypothesized that that eddy flux convergence of angular momentum during this period of time was large enough to offset the loss due to advection and still intensify the low-level mesocyclone. Thereafter, as the tornado continued to intensify, angular momentum within the low-level mesocyclone decreased. The low-level azimuthally averaged wind field continued to be divergent. Future work will endeavor to compute angular momentum budgets for tornadic and nontornadic hook

echoes to better understand how the evolution of angular momentum impacts the tornado and low-level mesocyclone.

Acknowledgments. Research results presented herein were supported by the National Science Foundation under Grant ATM-0757714. Any opinions, findings, and conclusions or recommendations expressed in this publication are those of the authors and do not necessarily reflect the views of the National Science Foundation. The DOW radars are National Science Foundation Lower Atmospheric Observing Facilities supported by ATM-0734001. The DOW deployments in VORTEX2 have been supported by ATM-0910737 and ATM-0966095. Analysis of DOW data has been supported by ATM-0947235. VORTEX2 has been supported, in part, by ATM-0724318. Radar data were processed with the SOLOii and Integrated Data Viewer (IDV) maintained by the National Center for Atmospheric Research Earth Observing Laboratory and Unidata, respectively. Comments by three anonymous reviewers significantly improved an earlier version of this manuscript.

REFERENCES

- Agee, E. M., J. T. Snow, and P. R. Clare, 1976: Multiple vortex features in the tornado cyclone and the occurrence of tornado families. *Mon. Wea. Rev.*, **104**, 552–563.
- Alexander, C. R., and J. Wurman, 2005: The 30 May 1998 Spencer, South Dakota, storm. Part I: The evolution and environment of the tornadoes. *Mon. Wea. Rev.*, **133**, 72–96.

- , and —, 2008: Updated mobile radar climatology of supercell tornado structures and dynamics. Preprints, *24th Conf. on Severe Local Storms*, Savannah, GA, Amer. Meteor. Soc., 19.4. [Available online at <http://ams.confex.com/ams/pdfpapers/141821.pdf>.]
- Beck, J. R., J. L. Schroeder, and J. M. Wurman, 2006: High-resolution dual-Doppler analyses of the 29 May 2001 Kress, Texas, cyclic supercell. *Mon. Wea. Rev.*, **134**, 3125–3148.
- Bluestein, H. B., 1993: *Synoptic-Dynamic Meteorology in Mid-latitudes*. Vol. 2, *Observations and Theory of Weather Systems*, Oxford Press, 594 pp.
- , and W. P. Unruh, 1989: Observations of the wind field in tornadoes, funnel clouds, and wall clouds with a portable Doppler radar. *Bull. Amer. Meteor. Soc.*, **70**, 1514–1525.
- , and A. L. Pazmany, 2000: Observations of tornadoes and other convective phenomena with a mobile, 3-mm wavelength, Doppler radar: The spring 1999 field experiment. *Bull. Amer. Meteor. Soc.*, **81**, 2939–2951.
- , and S. G. Gaddy, 2001: Airborne pseudo-dual-Doppler analysis of a rear-inflow jet and deep convergence zone within a supercell. *Mon. Wea. Rev.*, **129**, 2270–2289.
- , —, D. C. Dowell, A. L. Pazmany, J. C. Galloway, R. E. McIntosh, and H. Stein, 1997: Doppler radar observations of storm-scale vortices in a supercell. *Mon. Wea. Rev.*, **125**, 1046–1059.
- , C. C. Weiss, and A. L. Pazmany, 2003: Mobile Doppler radar observations of a tornado in a supercell near Bassett, Nebraska, on 5 June 1999. Part I: Tornadogenesis. *Mon. Wea. Rev.*, **131**, 2954–296.
- , —, and —, 2004: The vertical structure of a tornado near Happy, Texas, on 5 May 2002: High-resolution, mobile, W-band, Doppler radar observations. *Mon. Wea. Rev.*, **132**, 2325–2337.
- , M. M. French, R. L. Tanamachi, S. Frasier, K. Hardwick, F. Junyent, and A. L. Pazmany, 2007a: Close-range observations of tornadoes in supercells made with a dual-polarization, X-band, mobile Doppler radar. *Mon. Wea. Rev.*, **135**, 1522–1543.
- , C. C. Weiss, M. M. French, E. M. Holthaus, R. L. Tanamachi, S. Frasier, and A. L. Pazmany, 2007b: The structure of tornadoes near Attica, Kansas, on 12 May 2004: High-resolution, mobile, Doppler radar observations. *Mon. Wea. Rev.*, **135**, 475–506.
- Brandes, E. A., 1977: Gust front evolution and tornado genesis as viewed by Doppler radar. *J. Appl. Meteor.*, **16**, 333–338.
- , 1978: Mesocyclone evolution and tornadogenesis: Some observations. *Mon. Wea. Rev.*, **106**, 995–1011.
- , 1981: Finestructure of the Del City–Edmond tornadic mesocirculation. *Mon. Wea. Rev.*, **109**, 635–647.
- , 1984: Vertical vorticity generation and mesocyclone sustenance in tornadic thunderstorms: The observational evidence. *Mon. Wea. Rev.*, **112**, 2253–2269.
- Burgess, D., M. Magsig, J. Wurman, D. Dowell, and Y. Richardson, 2002: A detailed WSR-88D and DOW radar analysis of the Oklahoma City tornado of 3 May 1999. *Wea. Forecasting*, **17**, 456–471.
- Davies-Jones, R. P., 1986: *Tornado Dynamics*. Vol. 2, *Thunderstorms: A Social and Technological Documentary*, 2nd ed. E. Kessler, Ed., University of Oklahoma Press, 197–236.
- , and H. E. Brooks, 1993: Mesocyclogenesis from a theoretical perspective. *The Tornado: Its Structure, Dynamics, Prediction, and Hazards*, *Geophys. Monogr.*, Vol. 79, Amer. Geophys. Union, 105–114.
- , R. J. Trapp, and H. B. Bluestein, 2001: Tornadoes and tornadic storms. *Severe Convective Storms, Meteor. Monogr.*, No. 28, Amer. Meteor. Soc., 167–222.
- Dowell, D. C., and H. B. Bluestein, 1997: The Arcadia, Oklahoma, storm of 17 May 1981: Analysis of a supercell during tornadogenesis. *Mon. Wea. Rev.*, **125**, 2562–2582.
- , and —, 2002a: The 8 June 1995 McLean, Texas, storm. Part I: Observations of cyclic tornadogenesis. *Mon. Wea. Rev.*, **130**, 2626–2648.
- , and —, 2002b: The 8 June 1995 McLean, Texas, storm. Part II: Cyclic tornado formation, maintenance, and dissipation. *Mon. Wea. Rev.*, **130**, 2649–2670.
- , C. R. Alexander, J. M. Wurman, and L. J. Wicker, 2005: Centrifuging of hydrometeors and debris in tornadoes: Radar-reflectivity patterns and wind measurement errors. *Mon. Wea. Rev.*, **133**, 1501–1524.
- Frame, J., P. Markowski, Y. Richardson, J. Straka, and J. Wurman, 2009: Polarimetric and dual Doppler radar observations of the Lipscomb County, Texas, supercell thunderstorm on 23 May 2002. *Mon. Wea. Rev.*, **137**, 544–561.
- French, M. M., H. B. Bluestein, D. C. Dowell, L. J. Wicker, M. R. Kramar, and A. L. Pazmany, 2008: High-resolution, mobile Doppler radar observations of cyclic mesocyclogenesis in a supercell. *Mon. Wea. Rev.*, **136**, 4997–5016.
- Fujita, T. T., 1981: Tornadoes and downbursts in the context of generalized planetary scales. *J. Atmos. Sci.*, **38**, 1511–1534.
- , and R. M. Wakimoto, 1982: Anticyclonic tornadoes in 1980 and 1981. Preprints, *12th Conf. on Severe Local Storms*, San Antonio, TX, Amer. Meteor. Soc., 213–216.
- Klemp, J. B., and R. Rotunno, 1983: A study of the tornadic region within a supercell thunderstorm. *J. Atmos. Sci.*, **40**, 359–377.
- Koch, S. E., M. DesJardins, and P. J. Kocin, 1983: An interactive Barnes objective map analysis scheme for use with satellite and conventional data. *J. Climate Appl. Meteor.*, **22**, 1487–1503.
- Kosiba, K., and J. Wurman, 2010: The three-dimensional axisymmetric wind field structure of the Spencer, South Dakota, 1998 tornado. *J. Atmos. Sci.*, **67**, 3074–3083.
- Lee, W.-C., and J. Wurman, 2005: The diagnosed structure of the Mulhall tornado. *J. Atmos. Sci.*, **62**, 2373–2393.
- Majcen, M., P. Markowski, Y. Richardson, D. Dowell, and J. Wurman, 2008: Multipass objective analysis of Doppler radar data. *J. Atmos. Oceanic Technol.*, **25**, 1845–1858.
- Markowski, P., E. Rasmussen, J. Straka, R. Davies-Jones, Y. Richardson, and R. J. Trapp, 2008: Vortex lines within low-level mesocyclones obtained from pseudo Doppler radar observations. *Mon. Wea. Rev.*, **136**, 3513–3535.
- , M. Majcen, Y. Richardson, J. Marquis, and J. Wurman, 2011a: Characteristics of the wind field in a trio of nontornadic low-level mesocyclones observed by the Doppler on Wheels radars. *Electron. J. Severe Storms Meteor.*, **6** (3), 1–48.
- , and Coauthors, 2011b: Observations from VORTEX 2: The pretornadic phase of the Goshen County, Wyoming, supercell. Preprints, *35th Int. Conf. on Radar Meteorology*, Pittsburgh, PA, Amer. Meteor. Soc., 8B.1. [Available online at <http://ams.confex.com/ams/35Radar/webprogram/Manuscript/Paper191881/radar35.pdf>.]
- Marquis, J., Y. Richardson, J. Wurman, and P. Markowski, 2008: Single- and dual-Doppler analysis of a tornadic vortex and surrounding storm-scale flow in the Crowell, Texas, supercell of 30 April 2000. *Mon. Wea. Rev.*, **136**, 5017–5043.
- Pauley, P. M., and X. Wu, 1990: The theoretical, discrete, and actual response of the Barnes objective analysis scheme for one- and two-dimensional fields. *Mon. Wea. Rev.*, **118**, 1145–1163.
- Rasmussen, E. N., and J. M. Straka, 2007: Evolution of low-level angular momentum in the 2 June 1995 Dimmitt, Texas, tornado cyclone. *J. Atmos. Sci.*, **64**, 1365–1378.

- , —, R. P. Davies-Jones, C. A. Doswell, F. H. Carr, M. D. Eilts, and D. R. MacGorman, 1994: Verification of the Origins of Rotation in Tornadoes Experiment: VORTEX. *Bull. Amer. Meteor. Soc.*, **75**, 995–1006.
- , R. Davies-Jones, and R. L. Holle, 2003: Terrestrial photogrammetry of weather images acquired in uncontrolled circumstances. *J. Atmos. Oceanic Technol.*, **20**, 1790–1803.
- Rotunno, R., and J. B. Klemp, 1985: On the rotation and propagation of simulated supercell thunderstorms. *J. Atmos. Sci.*, **42**, 271–292.
- Ryzhkov, A. V., T. J. Schuur, D. W. Burgess, and D. S. Zrnic, 2005: Polarimetric tornado detection. *J. Appl. Meteor.*, **44**, 557–570.
- Stout, G. E., and F. A. Huff, 1953: Radar records Illinois tornado genesis. *Bull. Amer. Meteor. Soc.*, **34**, 281–284.
- Tanamachi, R. L., H. B. Bluestein, W.-C. Lee, M. Bell, and A. Pazmany, 2007: Ground based velocity track display (GBVTD) analysis of W-band Doppler radar data in a tornado near Stockton, Kansas, on 15 May 1999. *Mon. Wea. Rev.*, **135**, 783–800.
- Thompson, R. L., R. Edwards, J. A. Hart, K. L. Elmore, and P. Markowski, 2003: Close proximity soundings within supercell environments obtained from the rapid update cycle. *Wea. Forecasting*, **18**, 1243–1261.
- Trapp, J. R., 1999: Observations of nontornadic low-level mesocyclones and attendant tornadogenesis failure during VORTEX. *Mon. Wea. Rev.*, **127**, 1693–1705.
- Wakimoto, R. M., and B. E. Martner, 1992: Observations of a Colorado tornado. Part II: Combined photogrammetric and Doppler radar analysis. *Mon. Wea. Rev.*, **120**, 522–543.
- , and C. Liu, 1998: The Garden City, Kansas, storm during VORTEX 95. Part II: The wall cloud and tornado. *Mon. Wea. Rev.*, **126**, 393–408.
- , and H. Cai, 2000: Analysis of a nontornadic storm during VORTEX 95. *Mon. Wea. Rev.*, **128**, 565–592.
- , W.-C. Lee, H. B. Bluestein, C.-H. Liu, and P. H. Hildebrand, 1996: ELDORA observations during VORTEX 95. *Bull. Amer. Meteor. Soc.*, **77**, 1465–1481.
- , C. Liu, and H. Cai, 1998: The Garden City, Kansas, storm during VORTEX 95. Part I: Overview of the storm's life cycle and mesocyclogenesis. *Mon. Wea. Rev.*, **126**, 372–392.
- , H. V. Murphey, D. C. Dowell, and H. B. Bluestein, 2003: The Kellerville tornado during VORTEX: Damage survey and Doppler radar analyses. *Mon. Wea. Rev.*, **131**, 2197–2221.
- , N. T. Atkins, and J. Wurman, 2011: The LaGrange tornado during VORTEX2. Part I: Photogrammetric analysis of the tornado combined with single-Doppler radar data. *Mon. Wea. Rev.*, **139**, 2233–2258.
- Wood, V. T., R. A. Brown, and D. C. Dowell, 2009: Simulated WSR-88D velocity and reflectivity signatures of numerically modeled tornadoes. *J. Atmos. Oceanic Technol.*, **26**, 876–893.
- Wurman, J., and S. Gill, 2000: Finescale radar observations of the Dimmitt, Texas (2 June 1995), tornado. *Mon. Wea. Rev.*, **128**, 2135–2164.
- , and C. Alexander, 2005: The 30 May 1998 Spencer, South Dakota, storm. Part II: Comparison of observed damage and radar-derived winds in the tornadoes. *Mon. Wea. Rev.*, **133**, 97–119.
- , J. Straka, and E. Rasmussen, 1996: Fine scale Doppler radar observation of tornadoes. *Science*, **272**, 1774–1777.
- , —, —, M. Randall, and A. Zahrai, 1997: Design and deployment of a portable, pencil-beam, pulsed, 3-cm Doppler radar. *J. Atmos. Oceanic Technol.*, **14**, 1502–1512.
- , C. Alexander, P. Robinson, and Y. Richardson, 2007a: Low-level winds in tornadoes and potential catastrophic tornado impacts in urban areas. *Bull. Amer. Meteor. Soc.*, **88**, 31–46.
- , Y. Richardson, C. Alexander, S. Weygandt, and P.-F. Zhang, 2007b: Dual-Doppler and single-Doppler analysis of a tornadic storm undergoing mergers and repeated tornadogenesis. *Mon. Wea. Rev.*, **135**, 736–758.
- , —, —, —, and —, 2007c: Dual-Doppler analysis of winds and vorticity budget terms near a tornado. *Mon. Wea. Rev.*, **135**, 2392–2405.
- , P. Robinson, C. Alexander, and K. A. Kosiba, 2008: Rapid-scan mobile radar 3D GBVTD and traditional analysis of tornadogenesis. Preprints, *24th Conf. on Severe Local Storms*, Savannah, GA, Amer. Meteor. Soc., P13.6. [Available online at http://ams.confex.com/ams/24SLS/techprogram/paper_142176.htm.]
- , H. Bluestein, D. Burgess, D. Dowell, P. Markowski, Y. Richardson, and L. Wicker, 2010: VORTEX2: The Verification of the Origins of Rotation in Tornadoes Experiment. *Proc. Sixth European Conf. on Radar Meteorology and Hydrology*, Sibiu, Romania, European Meteorological Society, 10 pp. [Available online at http://www.erad2010.org/pdf/oral/wednesday/mesoscale/02_ERAD2010_0160.pdf.]
- Zehnder, J. A., J. Hu, and A. Razdan, 2007: A stereo photogrammetric technique applied to orographic convection. *Mon. Wea. Rev.*, **135**, 2265–2277.